Collapsing Response of a Nonlinear Shear-Beam Building Model Excited by a Strong-Motion Pulse at Its Base

Hamid Abbasgholiha [1], Vlado Gičev [2], Mihailo D. Trifunac [3], Reza S. Jalali [1] and Maria I. Todorovska [3,4,*]

[1] Faculty of Engineering, Department of Civil Engineering, University of Guilan, Rasht P.O. Box 3756, Iran
[2] Department of Computer Science, University Goce Delčev, Goce Delčev 89, 2000 Štip, North Macedonia
[3] Department of Civil and Environmental Engineering, University of Southern California, Los Angeles, CA 90089-2531, USA
[4] School of Civil Engineering, Tianjin University, 135 Yaguan Road, Tianjin 300350, China
[*] Correspondence: mtodorov@usc.edu or mtodorov@tju.edu.cn

Abstract: We present a simple nonlinear model of a shear-beam building that experiences large nonlinear deformations and collapse when excited by large pulses of strong earthquake ground motion. In this paper, we introduce the model and show that its properties can be selected to be consistent with the damage observed in a seven-story hotel in San Fernando Valley of the Los Angeles metropolitan area during the 1994 Northridge earthquake. We also show an example of excitation that leads to the collapse of the model. We illustrate the response only for a sequence of horizontal pulses. We will describe the response of the same model to horizontal, vertical, and rocking motions at its base, as well as for more general excitation by strong earthquake ground motion, in future papers.

1. Introduction

Buildings exposed to extreme events (earthquakes, tsunami, hurricanes, explosions, vehicle impact, fires, and terrorist attacks) may experience damage to key structural components that can lead to complete collapse. Examples include Ronan Point (London, 1968), the Capitan Arenas (Barcelona, 1972), the Argentine Israelite Mutual Association (Buenos Aires, 1994), the Murrah Federal Building (Oklahoma, 1995), the Sampoong Department store (Seoul, 1995), the World Trade Center (New York, 2001), and the Achimota Melcom Shopping Centre (Acra, 2012). These events have emphasized the need to design resilient buildings that can undergo considerable damage without experiencing complete collapse. Ideally, these buildings would be able to survive an extreme event in order to maintain functionality and enable the restoration of a pre-event performance. As such, it becomes essential to understand the geometrical and mechanical sequences of collapse in some detail.

Engineering analyses of collapsing structural models and proposed solutions for resilient design started to appear in publications around 2000, and the number of such studies continues to grow. The papers describe design methods to prevent collapse in different structural systems, in terms of three widely used approaches: tying force prescriptive rules, alternative load path (ALP) methods, and key element design methods [1]. The ALP method, which begins with the sudden removal of a key load-carrying member, has been used in analyses of modular high-rise buildings [2,3], steel buildings [4], and reinforced concrete (RC) buildings [5,6]. Recorded and observed collapses during the demolition of buildings have been used to verify the accuracy of computer simulations [7,8].

Before the era of modern earthquake engineering (circa early 1900s), traces of partial and complete collapse of various stone structures caused by strong earthquake shaking could be seen at numerous archeological sites. However, since the 1930s, when the first strong motion accelerographs were introduced [9], the complete collapse of a building by strong earthquake shaking has not been recorded. At the present time, although many instrumented structures exist in the world, only a few have experienced early stages of damage [10–13].

In the vicinity of earthquake faults, the destructive strong ground motion contains powerful pulses [14] and large permanent displacements [15,16] that can lead to large nonlinear responses and to structure collapse. For example, during the 1940 earthquake in Imperial Valley, California, field observations of strike-slip dislocations on the surface-fault rupture showed displacement amplitudes in the range from 1 to 2 m. At Cocopah, the observed fault slip was 3.5 m and 5 m at the All American Canal [15]. During the 1971 San Fernando earthquake, the rupture started at a depth of 9 km with a dislocation amplitude of 10 m. The dislocation then propagated up along the fault with a velocity of 2 km/s and diminishing slip amplitudes to 1 m. Before reaching the surface, the dislocation increased to near 6 m. Field observations in the San Fernando Valley of the surface-fault breaks showed strike-slip displacements of 0.5 to 1 m up and 0.8 to 1.7 m strike-slip displacements. During the San Fernando earthquake, the fault motion lasted about 9 s [16]. During the 1994 Northridge earthquake, the slip started at a depth of 17.5 km with a slip of about 3 m. The dislocation then propagated up toward the northwest and west and stopped at a depth of 5 km. The fault length was 18 km, with a width of 24 km. The faulting lasted about 6 s [17]. Figure 1 shows the central San Fernando Valley and the site of the Van Nuys seven-story hotel (VN7SH). The dashed lines represent horizontal projections of the faults of the 1971 San Fernando and 1994 Northridge, California, earthquakes. The duration of faulting during these two earthquakes was about 9 and 6 s, respectively. Directions and arrows show the distances to the seven earthquakes (see Table 3.1 in [18]). The solid stars show the epicenters of two Northridge aftershocks.

At present, there are no publications that describe the numerical simulation of the response of three-dimensional building models through all stages of geometrically non-linear response leading to collapse caused by strong earthquake shaking [1]. The buildings in which the early stages of nonlinear response have been recorded have provided a full-scale experimental basis for studies on the onset of nonlinearity in the soil and in the structure [10,19-21]. Studies on the nonlinear response of simple beam models of buildings, excited by strong motion pulses, have helped to point out to locations along the building height at which nonlinear deformations would be initiated [22–24]. Such studies have led to the successful identification of the locations at which damage has been initiated in actual buildings, as confirmed by post-earthquake site visits [24].

This paper aims to contribute to the understanding of how large amplitude pulses of ground motion might lead to the collapse of buildings deforming predominantly in shear using the numerical simulation of the nonlinear response of a simple building model, considering both material and geometric nonlinearities. Building collapse is a complex and highly nonlinear process in which the structural system and foundation soil interact simultaneously, while the principle of superposition does not apply. To begin to understand some of the basic features of this process, we conducted a controlled numerical experiment and considered only the most elementary example of a shear beam supported by rigid soil, i.e., neglecting phenomena associated with the soil–structure interaction. At this stage, we considered only a horizontal strong-motion pulse at the base. The response of the model was computed by a finite difference scheme. This study, however, differs from our previous closely related studies, which were also based on the simulation of the building response by the finite-differences method [23], in that the model also considers large deformations and the effects of gravity.

This paper is organized as follows. First, the Section 2.1 describes the case of a full-scale building damaged by earthquakes, based on which the simple model solved in this

paper has been constructed. Then, the Section 2.2 describes the model and method of solution. The Section 3 shows the results for displacements and strains along the height of the model, which point to the locations where collapse was initiated and show how it spread throughout the model. Finally, in the Section 4, the results are discussed, and the conclusions reached are presented.
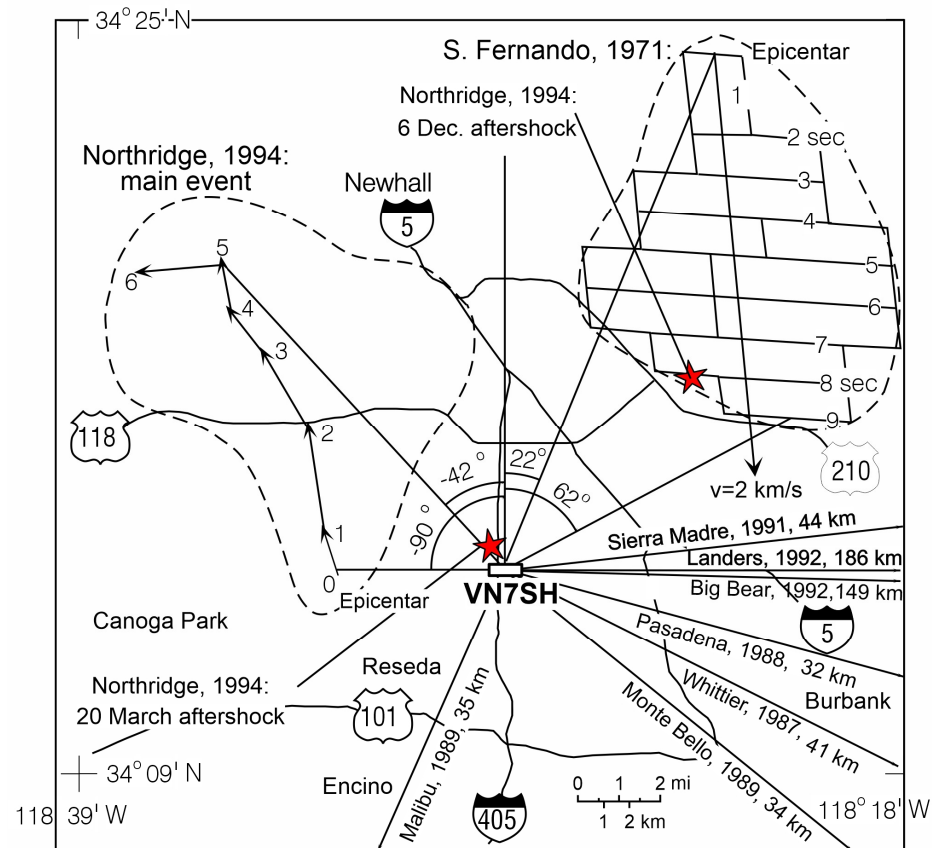
Figure 1. Location of Van Nuys seven-story hotel (VN7SH) and relative to the faults of the 1971 San Fernando and 1994 Northridge, California, earthquakes and other earthquakes recorded in the building [18].

2. Materials and Methods

2.1. Motivation

The number of instrumented buildings that have experienced some earthquake damage is limited and, as far as we know, no buildings with strong motion recorders have experienced collapse during earthquake shaking. Therefore, we used observations of the early stages of damage in the Van Nuys seven-story hotel building (VN7SH) to qualitatively illustrate the onset of damage as predicted by our model. We also considered hypothetical large amplitudes of ground motion to illustrate one possible path toward complete collapse of the building.

2.1.1. The Structure

VN7SH (Figure 2) was lightly damaged in the 1971 San Fernando earthquake and subsequently repaired. It was severely damaged in the 1994 Northridge earthquake (Figure 1) [25–29]. The building, which is 18.9 by 45.7 m in plan and 20 m high, was designed in 1965 and constructed in 1966 [30,31]. The typical framing consists of four rows of columns spaced on 6.1-m centers in a transverse direction and 5.7-m centers in a longitudinal direction (nine columns) (Figure 2). Spandrel beams surround the perimeter of the structure. Lateral forces in the longitudinal (EW) direction are resisted by interior column-slab

frames (B and C) and exterior column-spandrel beam frames (A and D). The added stiffness in the exterior frames associated with the spandrel beams creates exterior frames that are roughly twice as stiff as the interior frames. The floor system is a reinforced concrete flat slab that is 25.4-cm thick at the second floor, 21.6-cm thick at the third-to-seventh floors, and 20.3-cm thick at the roof [32–36]. The building is relatively stiff for shear deformations on the lowest two floors and more flexible between the third floor and roof (Figure 3) [24].
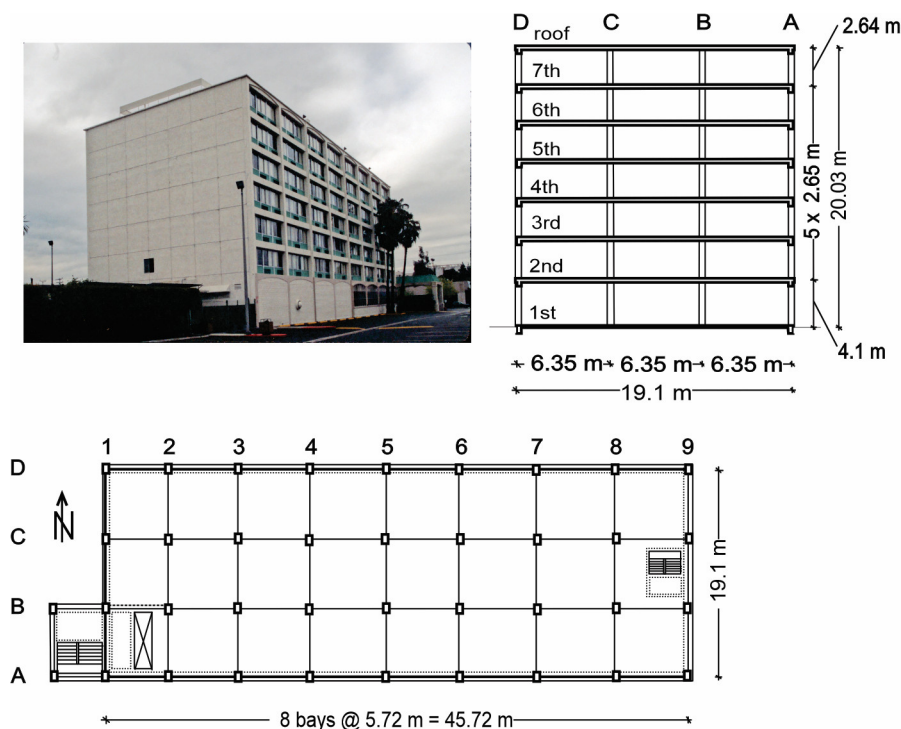
Figure 2. (**Top left**) View toward the southwest, (**top right**) typical transverse section, and (**bottom**) typical floor framing plan.

The building is situated on undifferentiated Holocene alluvium, uncemented and unconsolidated, with a thickness of less than 30 m, and an age of < 10,000 years [37,38]. The average shear-wave velocity in the top 30 m of soil is 300 m/s, and the soil-boring log shows that the underlying soil consists primarily of fine sandy silts and silty fine sands. The foundation system consists of 96.5-cm-deep pile caps supported by groups of two-to-four, poured-in-place, 61-cm-diameter, reinforced-concrete friction piles. These are centered under the main building columns, and all of the pile caps are connected by a grid of beams. Each pile is approximately 12.2-m long with a design capacity of over 444.82×10^3-N vertical load and up to 88.96×10^3-N lateral load. The structure is constructed of normal-weight reinforced concrete [30].
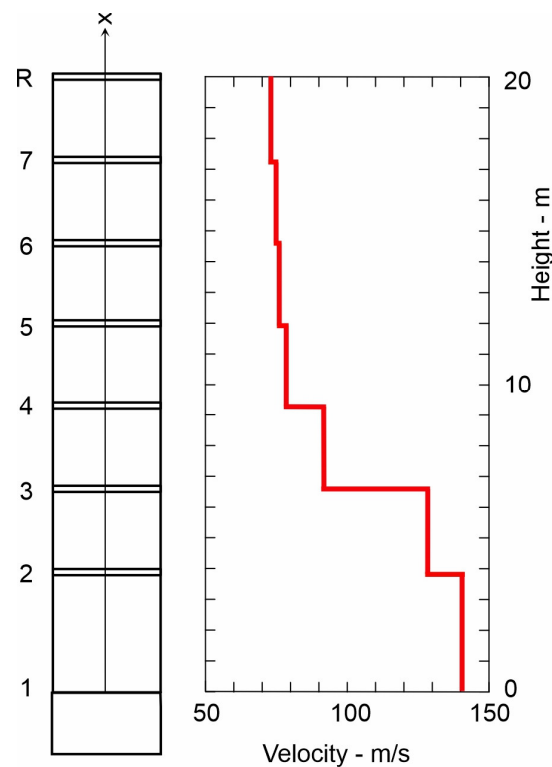
Figure 3. A layered model of the building and the velocity of shear waves in the layers determined by ambient vibration tests [27].

2.1.2. Earthquake Damage and Recorded Response

Although the M_L = 6.4 Northridge earthquake on 17 January 1994 severely damaged the building, its potential damage was probably reduced by the nonlinear response of soils in the area surrounding the building [37–43]. The structural damage was extensive in the exterior north (D) (Figure 2) and south (A) frames, which were designed to take most of the lateral load in the longitudinal (EW) direction. Severe shear cracks occurred in the middle columns of frame A, near the contact with the spandrel beam just below the fifth floor (Figure 4), and these cracks significantly decreased the axial, moment, and shear capacity of the columns. The shear cracks that appeared in the north (D) frame caused minor-to-moderate changes in the capacities of these structural elements. No major damage to the interior longitudinal (B and C) frames was observed, and there was no visible damage to the slabs or around the foundation. The nonstructural damage was significant. Photographs and detailed descriptions of the damage from the earthquake can be found in [18,28,29]. An analysis of the relationship between the observed damage and the changes in equivalent shear-wave velocity along the building height can be found in [11,27]. A discussion of the extent to which this damage has contributed to the changes in the apparent period of the soil–structure system can be found in [12,13].
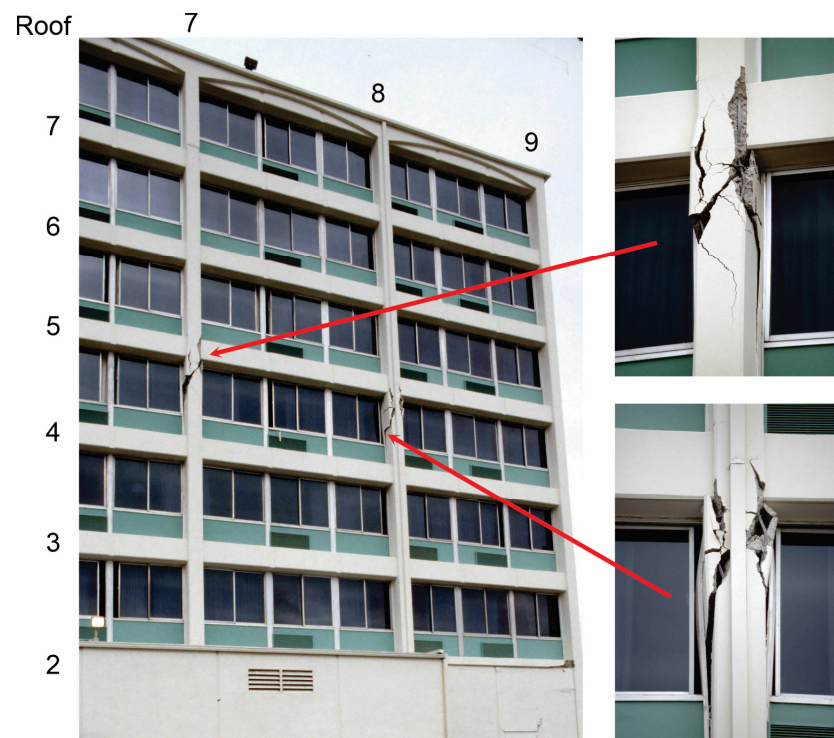
Figure 4. View of damaged columns A7 and A8 in frame A on the north side of the building after the Northridge earthquake (see Figure 2) [18].

Accelerations during the 1994 Northridge earthquake were recorded by a 13-channel CR-1 central recording system and one tri-axial SMA-1 accelerograph with an independent recording system, which had a common trigger time with the CR-1 recorder [18,44]. Figure 5 shows the first 25 s of recorded strong-motion displacements in the EW direction, which corresponds to the longitudinal direction in this building. In this paper, we considered only the longitudinal (EW) response of the building because it was the least affected by the soil–structure interaction, enabling us to approximately analyze its response via a simplified 1D, layered, shear-beam model. The motion in the building was recorded at the ground; at the second, third, and sixth floors; and at the roof. The five highlighted peaks in the recorded ground displacement, all acting in the same direction, were used in this paper as a guide to adopt simplified excitation by five half-sine pulses, which are shown at the bottom of the figures presenting the results of this study. In future generalizations of this work and associated sensitivity studies, we will consider various combinations of pulses differing in their total number, relative amplitudes, directions of action, and duration.
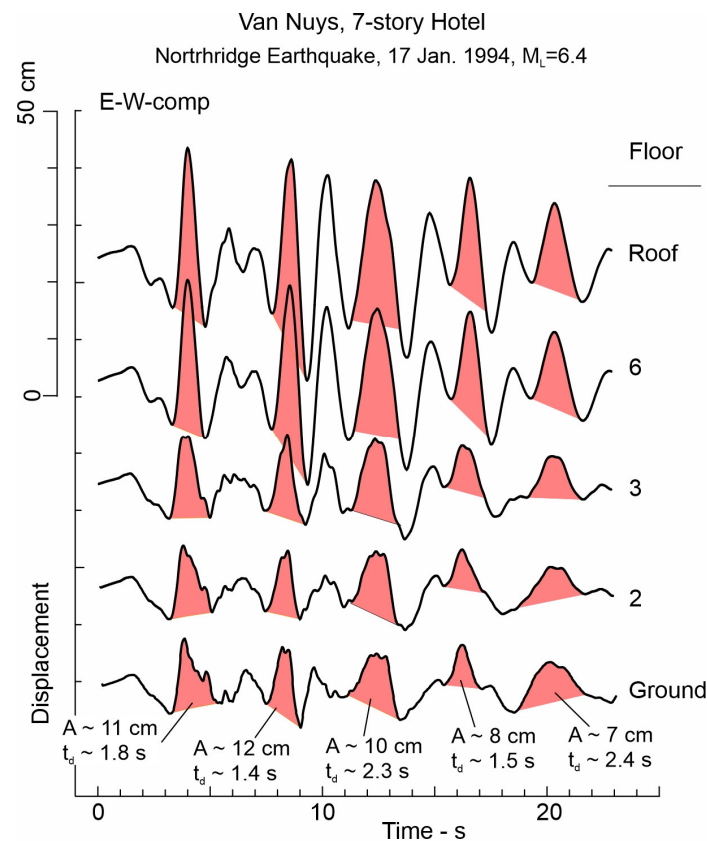
Figure 5. The first 25 s of the EW recorded earthquake displacements in VN7SH at a ground level; the second, third, and sixth floors; and at the roof. Pulses are emphasized by shades in the recorded motion at the ground level, with amplitudes A~11, 12, 10, 8, and 7 cm; durations 1.8, 1.4, 2.3, 1.5, and 2.4 s; at 3.1, 7.8, 11.2, 15.6, and 19.1 s after the trigger, respectively, and propagated up the building.

2.2. Method

2.2.1. Model

Our goal is to explore the complexities of nonlinear building response through all of the stages that led to the building's collapse. As this is a highly nonlinear problem, we will approach it in stages by first considering the most elementary models and then progressing toward more realistic ones. To this end, in this paper, we described only the nonlinear collapsing model consisting of a shear building. We assumed that earthquake ground motion was only horizontal. We ignored the vertical and rocking ground motions and assumed that there was no soil–structure interaction.

We considered a 1D shear-building model (Figure 6a) excited by a horizontal half-sine pulse at its base (Figure 6b). We present equations that consider both horizontal and vertical motion at the building base, but in this paper, we showed the results only for excitation by a horizontal pulse. The density and shear wave velocity in the building varied with height and are given in Table 1, with values motivated by the VN7SH building, which we previously investigated. We assumed that the base of our model is rigid, i.e., there is no soil–structure interaction, and that during the ground displacement the base (point 1) moves horizontally with displacement $u(t)$, which is a pulse-like motion. In all of the results in this paper, we used $H_b = 20.036$ m and $\varepsilon_{yb} = 0.0025$ for the maximum linear strain in the bilinear stress–strain relationship, with second slope $\gamma = 0.44$ (Figure 7). To enable qualitative comparison with previous studies of the nonlinear response of the VN7SH building, this stress–strain relationship has been selected based on several response analyses using simplified engineering push-over methods, reviewed,

interpreted, and then adopted as in [22]. The average shear-wave velocity in the building was computed as $\beta_b = H_b / \sum_{i=1}^{7} \frac{h_i}{\beta_i} = 91.79$ m/s, where h_i and β_i are the height and shear-wave velocity, respectively, in the i-th building layer.

Table 1. One dimensional VN7SH model assumed to be fixed at its base.

	Story Height (m) h_i	Number of Spatial Intervals in Each Story	β_i (m/s)	ρ_i (kg/m³)
First story	3.987	59	140.20	76.92
Second story	2.675	39	129.50	82.90
Third story	2.656	39	91.44	82.90
Fourth story	2.656	39	79.25	82.90
Fifth story	2.656	39	77.72	82.90
Sixth story	2.6555	39	76.20	82.90
Seventh story	2.7505	40	73.15	82.90
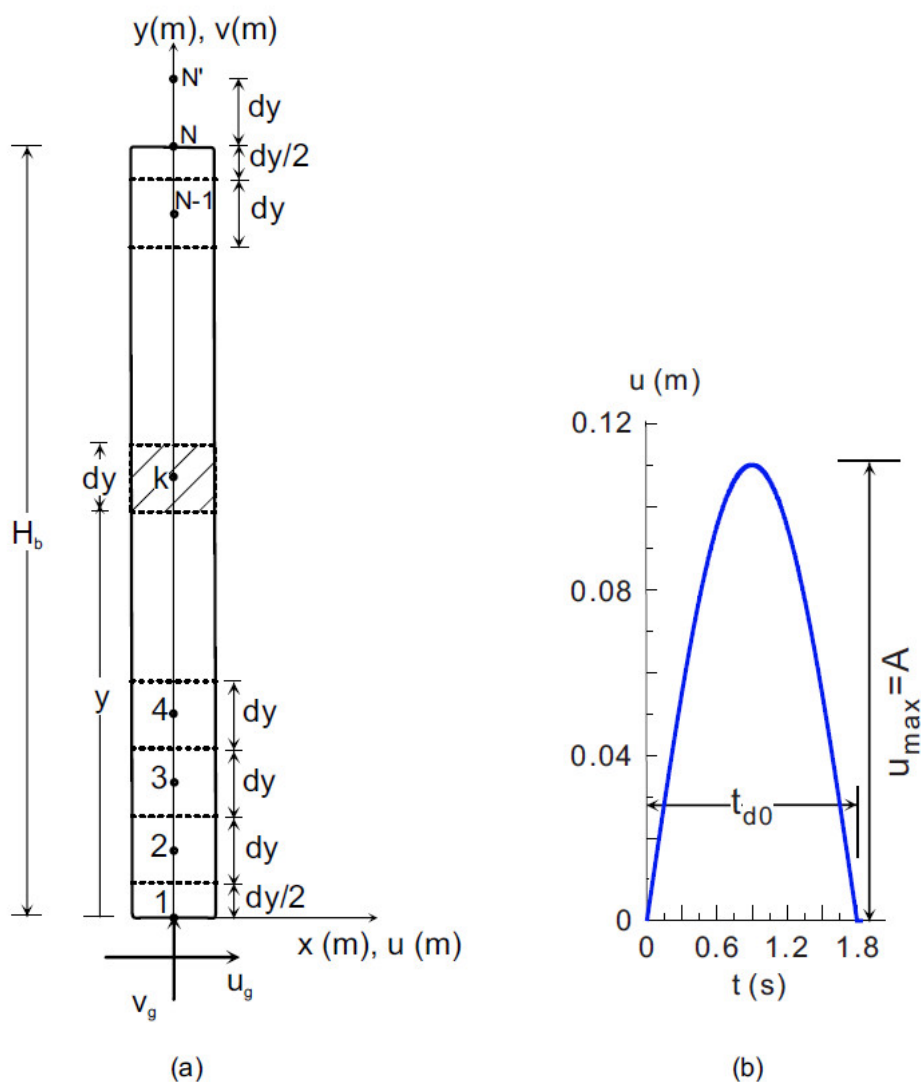
Figure 6. (**a**) The model, a shear building with a fixed base. (**b**) The input horizontal ground motion pulse.
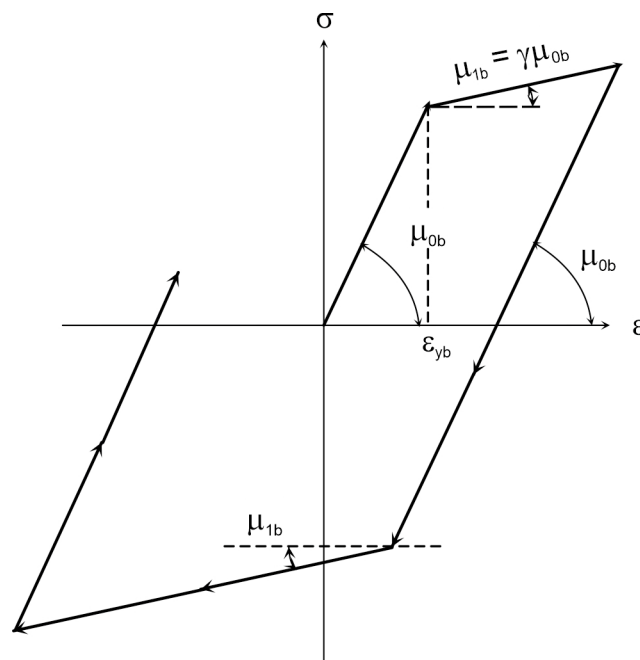
Figure 7. The constitutive law for the shear-building material.

We considered a model with continuously varying stiffness, determined from ambient vibration tests [27]. Because the measurements could not resolve the stiffness associated with the individual structural members, the floor slabs were not modeled explicitly. The model was discretized into 294 spatial intervals, so that the top point N of the building in Figure 6a is the 295th point of the model. Above this point, in order to facilitate the computation of the spatial derivative in the numerical calculations, an additional dummy point N' is introduced at distance dy, which will be the 296th point of the model. The constitutive law of the building material $\sigma = \sigma(\varepsilon)$ is bilinear (Figure 7).

2.2.2. Equations of Motion

To derive the equations of motion of the model, we considered an arbitrary point of the building, k, in arbitrary time, t (Figure 8). The active forces per unit volume acting on element k are the inertial body forces $\rho\ddot{u}$ and $\rho\ddot{v}$, and the self-weight ρg. The state of stress at element k consists of shear stress $\tau_{\xi\eta}$ and normal vertical stress σ_y. Because of these forces, element k undergoes shear deformation ε_k at time t. The translational motion of point k consists of horizontal motion u, and vertical motion v (Figure 8).

From Figure 8, $d\xi = dy \cos\varepsilon_k$ and the area $A' = \Delta x \, \Delta z = 1$ and the relation between the derivatives with respect to y and ξ are

$$\frac{\partial}{\partial \xi} = \frac{\partial}{\partial y}\frac{dy}{d\xi} = \frac{1}{\cos\varepsilon_k}\frac{\partial}{\partial y} \tag{1}$$

From the free-body diagram of element k (Figure 8)

$$\sum F_x = 0 \quad \Rightarrow \quad \left(\tau_{\xi\eta} + \frac{\partial \tau_{\xi\eta}}{\partial \xi}dy - \tau_{\xi\eta}\right)A' - \rho A'\left(dy\cos\varepsilon_k\right)\frac{\partial v_x}{\partial t} = 0 \tag{2}$$

In Equation (2), we introduced the transformation from the $x - y$ to the $\xi - \eta$ coordinate system, in which coordinate ξ has origin at the center of element k and is oriented in its longitudinal direction, while coordinate η drops out because the model is

1D, including transformation of the derivatives using Equation (1), and division by $A'dy$ gives

$$\frac{\partial v_x}{\partial t} = \frac{1}{\rho \cos^2 \varepsilon_k} \frac{\partial \tau_{\xi\eta}}{\partial y} \tag{3}$$

Similarly, from the free body diagram of element k (Figure 8)

$$\sum F_y = 0 \quad \Rightarrow \left(\sigma_y + \frac{\partial \sigma_y}{\partial \xi} dy - \sigma_y \right) A' - \rho A' \left(dy \cdot \cos \varepsilon_k \right) \left(\frac{\partial v_y}{\partial t} + g \right) = 0 \tag{4}$$

and Equation (4) becomes

$$\frac{\partial v_y}{\partial t} = \frac{1}{\rho \cos^2 \varepsilon_k} \frac{\partial \sigma_y}{\partial y} - g \tag{5}$$

Equations (3) and (5) represent the equations of motion for element k.
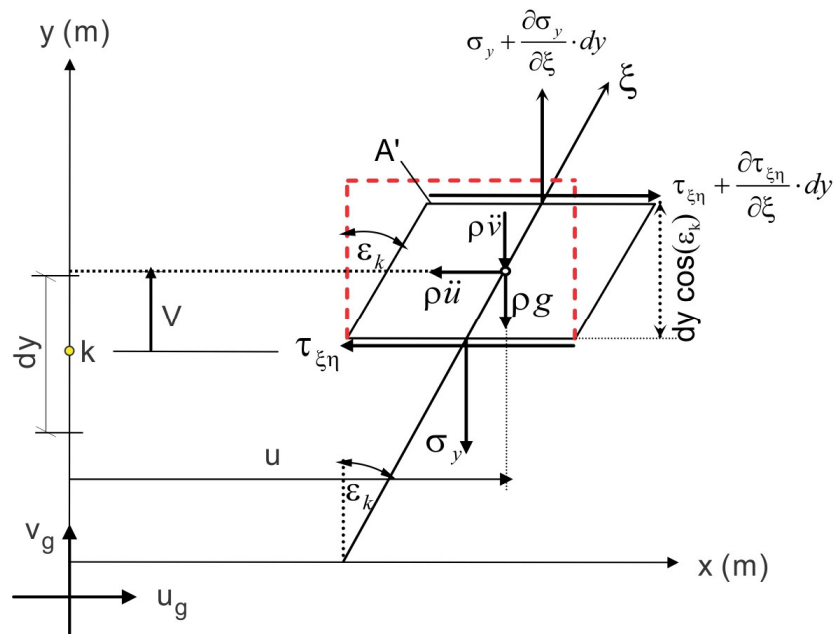

Figure 8. The free body diagram of element k.

2.2.3. Compatibility Conditions

We introduce a connecting element k, such that it connects points k and $k+1$, as shown in Figure 9, which has length dy and is characterized only by its angular velocity ω and rotation ε_k. We use this element to derive the compatibility relation between the motions of the two points based on the principles of the kinematics of rigid bodies.
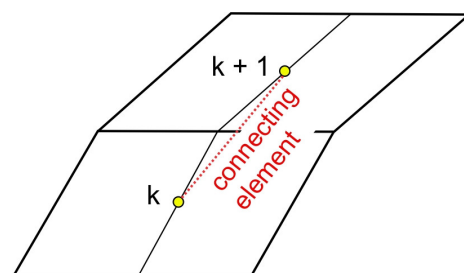

Figure 9. The connecting element between two points, k and $k+1$.

Figure 10 shows the parameters used in the computation of the compatibility relation. Part (a) shows the horizontal and vertical components, $V_{k,x}$, $V_{(k+1),x}$, $V_{k,y}$, and $V_{(k+1),y}$, of the velocity vector at points k and $k+1$, $\vec{V}_k$ and $\vec{V}_{k+1}$. The angular velocity and rotation of the connecting element, ω and ε_k, and the relative velocity vector, $\vec{V}_{(k+1)/k}$, between points k and $k+1$, are shown in part (b). The orientations of the axes and unit vectors are shown in part (c), while part (d) shows the orientation of the angular velocities and velocity vectors. The horizontal and vertical velocities of the two points, k and $k+1$, are related to each other through the angular velocity of the connecting element, ω.
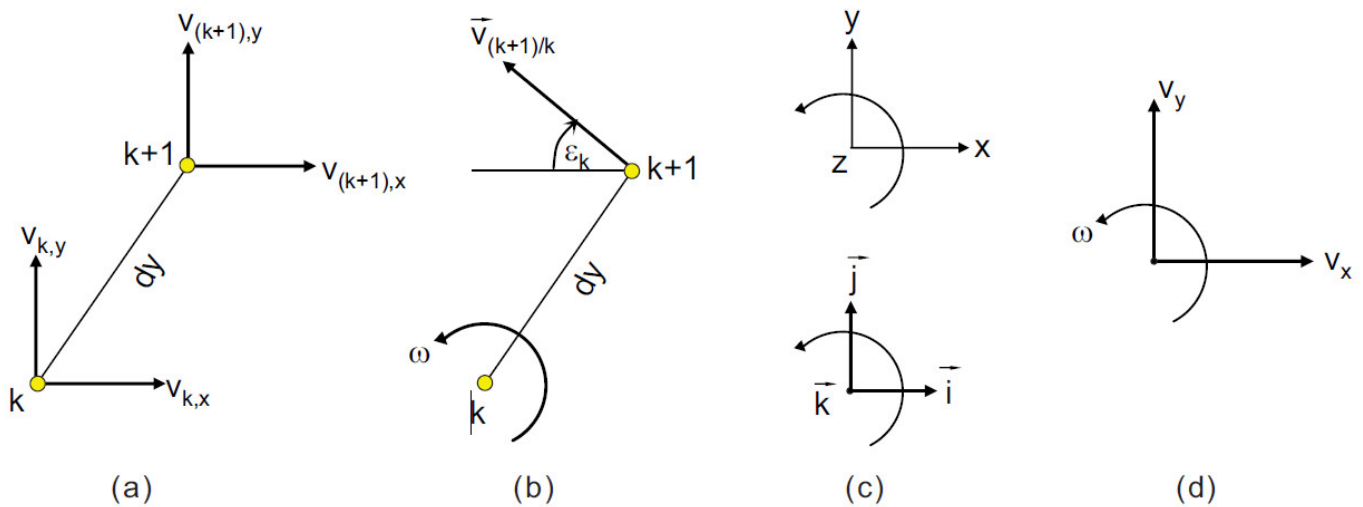
Figure 10. (**a**) The definition of the horizontal and vertical velocities; (**b**) rotation, angular velocity and relative velocity in the connecting element as a rigid body; (**c**) convention of axes and unit vectors; and (**d**) convention of horizontal and vertical velocity vectors and angular velocity.

Based on the convention in Figure 10d, ω is positive counterclockwise. However, we adopted a convention such that ε_k and $\dot{\varepsilon}_k$ are positive if clockwise, which implies $\dot{\varepsilon}_k = -\omega$. The position vector $\vec{r}$, is defined as the vector that originated at point k and ending at point $k+1$ and has length dy. Based on the kinematics of rigid bodies, the following relations between the velocities at k and $k+1$ and the relative velocity, $\vec{V}_{(k+1)/k}$, can be obtained

$$\vec{V}_{k+1} = \vec{V}_k + \vec{V}_{(k+1)/k} = \vec{V}_k + \omega \vec{k} \times \vec{r} \tag{6}$$

$$V_{(k+1),x}\vec{i} + V_{(k+1),y}\vec{j} = V_{k,x}\vec{i} + V_{k,y}\vec{j} - \omega|\vec{r}|\cos\varepsilon_k\vec{i} + \omega|\vec{r}|\sin\varepsilon_k\vec{j} \tag{7}$$

in which

$$\omega = -\dot{\varepsilon}_k \quad , \quad |\vec{r}| = dy \tag{8}$$

Substituting Equation (8) into Equation (7) and defining $\dfrac{\partial v_x}{\partial y} = \dfrac{V_{(k+1),x} - V_{k,x}}{dy}$ and

$\dfrac{\partial v_y}{\partial y} = \dfrac{V_{(k+1),y} - V_{k,y}}{dy}$ gives

$$\frac{\partial v_x}{\partial y}\vec{i} + \frac{\partial v_y}{\partial y}\vec{j} = \dot{\varepsilon}_k \left(\cos \varepsilon_k \vec{i} - \sin \varepsilon_k \vec{j} \right) \tag{9}$$

Taking dot product of each side of Equation (9) with $\left(\cos \varepsilon_k \vec{i} - \sin \varepsilon_k \vec{j} \right)$ gives

$$\left(\frac{\partial v_x}{\partial y}\vec{i} + \frac{\partial v_y}{\partial y}\vec{j} \right) \cdot \left(\cos \varepsilon_k \vec{i} - \sin \varepsilon_k \vec{j} \right) = \dot{\varepsilon}_k \tag{10}$$

and

$$\dot{\varepsilon}_k = \frac{\partial v_x}{\partial y}\cos \varepsilon_k - \frac{\partial v_y}{\partial y}\sin \varepsilon_k \tag{11}$$

Equation (11) constitutes the compatibility equation for the element, which relates the horizontal and vertical velocities of points k and $k+1$ (Figure 10). It is noted that, in the absence of such compatibility condition, velocities $\partial v_x / \partial t$ and $\partial v_y / \partial t$, specified in Equations (3) and (5), would be independent.

2.2.4. The Finite Differences Scheme

The Lax–Wendroff [45] $O(dt^2, dy^2)$ finite difference method for a set of simultaneous equations is used to solve the problem. Equations (3), (5) and (11) can be written in matrix form as

$$\left[\mathbf{U}_{,t} \right]_{3\times 1} = \left[\mathbf{B} \right]_{3\times 2} \left[\mathbf{F}_{,y} \right]_{2\times 1} + \left[\mathbf{G} \right]_{3\times 1} \tag{12}$$

in which

$$\mathbf{U} = \begin{Bmatrix} v_x \\ v_y \\ \varepsilon_k \end{Bmatrix}, \quad \mathbf{F} = \begin{Bmatrix} \tau_{\xi\eta} \\ \sigma_y \end{Bmatrix}, \quad \mathbf{G} = \begin{Bmatrix} 0 \\ -g \\ \dfrac{\partial v_x}{\partial y}\cos \varepsilon_k - \dfrac{\partial v_y}{\partial y}\sin \varepsilon_k \end{Bmatrix},$$

$$\mathbf{B} = \begin{bmatrix} \dfrac{1}{\rho \cos^2 \varepsilon_k} & 0 \\ 0 & \dfrac{1}{\rho \cos^2 \varepsilon_k} \\ 0 & 0 \end{bmatrix} \tag{13}$$

Expanding $\mathbf{U}$ in Taylor series up to the third term gives

$$\mathbf{U}_{k,n+1} = \mathbf{U}_{k,n} + \Delta t \left(\frac{\partial \mathbf{U}}{\partial t} \right)_{k,n} + \frac{\Delta t^2}{2} \left(\frac{\partial^2 \mathbf{U}}{\partial t^2} \right)_{k,n} + O\left(\Delta t^3 \right) \tag{14}$$

The substitution of Equation (12) into Equation (14) gives

$$\mathbf{U}_{k,n+1} = \mathbf{U}_{k,n} + \Delta t \left(\mathbf{B}\frac{\partial \mathbf{F}}{\partial y} + \mathbf{G} \right)_{k,n} + \frac{\Delta t^2}{2}\frac{\partial}{\partial t}\left(\mathbf{B}\frac{\partial \mathbf{F}}{\partial y} + \mathbf{G} \right)_{k,n} + O\left(\Delta t^3 \right) \tag{15}$$

In which

$$\frac{\partial}{\partial t}\left(\mathbf{B}\,\frac{\partial \mathbf{F}}{\partial y} + \mathbf{G}\right) = \left(\frac{\partial}{\partial t}\,\mathbf{B}\right)\frac{\partial \mathbf{F}}{\partial y} + \mathbf{B}\,\frac{\partial}{\partial t}\,\frac{\partial \mathbf{F}}{\partial y} + \frac{\partial}{\partial t}\,\mathbf{G} \tag{16}$$

$$\frac{\partial}{\partial t}\,\frac{\partial \mathbf{F}}{\partial y} = \frac{\partial}{\partial y}\,\frac{\partial \mathbf{F}}{\partial t} = \frac{\partial}{\partial y}\left(\frac{\partial \mathbf{F}}{\partial \mathbf{U}}\,\frac{\partial \mathbf{U}}{\partial t}\right) = \frac{\partial}{\partial y}\left[\mathbf{J}\left(\mathbf{B}\,\frac{\partial \mathbf{F}}{\partial y} + \mathbf{G}\right)\right] \tag{17}$$

And **J** is the Jacobian matrix

$$\mathbf{J} = \text{Jacobian}(\mathbf{F}) = \frac{\partial \mathbf{F}}{\partial \mathbf{U}} = \begin{bmatrix} \dfrac{\partial \tau_{\xi\eta}}{\partial v_x} & \dfrac{\partial \tau_{\xi\eta}}{\partial v_y} & \dfrac{\partial \tau_{\xi\eta}}{\partial \varepsilon} \\[2ex] \dfrac{\partial \sigma_y}{\partial v_x} & \dfrac{\partial \sigma_y}{\partial v_y} & \dfrac{\partial \sigma_y}{\partial \varepsilon} \end{bmatrix} = \begin{bmatrix} 0 & 0 & \dfrac{\partial \tau_{\xi\eta}}{\partial \varepsilon} \\[2ex] 0 & 0 & \dfrac{\partial \sigma_y}{\partial \varepsilon} \end{bmatrix} \tag{18}$$

Finally, Equation (15) for point k of the model and time step n of the analysis becomes

$$\mathbf{U}_{k,n+1} = \mathbf{U}_{k,n} + \frac{\Delta t}{\rho}\,\mathbf{C}_{k,n} + \frac{\Delta t^2}{2\rho}\,\mathbf{D}_{k,n} + \frac{\Delta t^2}{2\rho}\,\mathbf{E}_{k,n} \tag{19}$$

in which

$$\mathbf{C}_{k,n} = \left\{ \begin{array}{c} \dfrac{1}{\cos^2 \varepsilon_k}\,\dfrac{\partial \tau_{\xi\eta}}{\partial y} \\[2ex] \dfrac{1}{\cos^2 \varepsilon_k}\,\dfrac{\partial \sigma_y}{\partial y} - \rho g \\[2ex] \rho\left(\dfrac{\partial v_x}{\partial y}\cos \varepsilon_k - \dfrac{\partial v_y}{\partial y}\sin\varepsilon_k\right) \end{array} \right\}_{k,n} \tag{20}$$

$$\mathbf{D}_{k,n} = \left\{ \begin{array}{c} \dfrac{1}{\cos^4 \varepsilon_k}\left[\sin(2\varepsilon_k)\left(\dfrac{\partial v_x}{\partial y}\cos \varepsilon_k - \dfrac{\partial v_y}{\partial y}\sin\varepsilon_k\right)\right]\left(\dfrac{\partial \tau_{\xi\eta}}{\partial y}\right) \\[2ex] \dfrac{1}{\cos^4 \varepsilon_k}\left[\sin(2\varepsilon_k)\left(\dfrac{\partial v_x}{\partial y}\cos \varepsilon_k - \dfrac{\partial v_y}{\partial y}\sin\varepsilon_k\right)\left(\dfrac{\partial \sigma_y}{\partial y}\right)\right] \\[2ex] \dfrac{\partial}{\partial y}\left(\dfrac{1}{\cos^2 \varepsilon_k}\,\dfrac{\partial \tau_{\xi\eta}}{\partial y}\right)\cos \varepsilon_k - \dfrac{\partial}{\partial y}\left(\dfrac{1}{\cos^2 \varepsilon_k}\,\dfrac{\partial \sigma_y}{\partial y}\right)\sin \varepsilon_k + \\[2ex] +\rho\left\{-\dfrac{\partial v_x}{\partial y}\,\dfrac{\partial v_y}{\partial y}\cos(2\varepsilon_k) - \dfrac{1}{2}\left[\left(\dfrac{\partial v_x}{\partial y}\right)^2 - \left(\dfrac{\partial v_y}{\partial y}\right)^2\right]\sin(2\varepsilon_k)\right\} \end{array} \right\}_{k,n} \tag{21}$$

$$\mathbf{E}_{k,n} = \left\{ \begin{array}{c} \dfrac{1}{\cos^2 \varepsilon_k}\,\dfrac{\partial}{\partial y}\left[\left(\dfrac{\partial v_x}{\partial y}\cos \varepsilon_k - \dfrac{\partial v_y}{\partial y}\sin\varepsilon_k\right)\dfrac{\partial \tau_{\xi\eta}}{\partial \varepsilon}\right] \\[2ex] \dfrac{1}{\cos^2 \varepsilon_k}\,\dfrac{\partial}{\partial y}\left[\left(\dfrac{\partial v_x}{\partial y}\cos \varepsilon_k - \dfrac{\partial v_y}{\partial y}\sin\varepsilon_k\right)\dfrac{\partial \sigma_y}{\partial \varepsilon}\right] \\[2ex] 0 \end{array} \right\}_{k,n} \tag{22}$$

2.2.5. Stresses, Boundary Conditions, and Displacements

The normal stress, σ_y, at each point and its derivative with respect to the strain, ε, are computed as

$$\left(\sigma_y\right)_{k,n+1} = -\sum_{j=k}^{294}\left\{\rho\cos^2\varepsilon_{j,n+1}\left[\left(\dot{v}_y\right)_{j,n+1} + g\right]\right\}dy_j \tag{23}$$

$$\left(\frac{\partial\sigma_y}{\partial\varepsilon}\right)_{k,n+1} = \sum_{j=k}^{294}\left\{\rho\sin\left(2\varepsilon_{j,n+1}\right)\left[\left(\dot{v}_y\right)_{j,n+1} + g\right]\right\}dy_j \tag{24}$$

For a stress-free point at the top of the shear building (point 295, see Figure 6), at all times, the velocities and stresses at the dummy point (296, see Figure 6) are updated as

$$\frac{\left(v_x\right)_{296,n} - \left(v_x\right)_{294,n}}{2dy} = 0 \quad\Rightarrow\quad \left(v_x\right)_{296,n} = \left(v_x\right)_{294,n} \tag{25}$$

$$\left(v_y\right)_{296,n} = \left(v_y\right)_{294,n} \tag{26}$$

$$\left(\sigma_y\right)_{296,n} = -\left(\sigma_y\right)_{294,n} \tag{27}$$

$$\left(\varepsilon\right)_{296,n} = -\left(\varepsilon\right)_{294,n} \quad\Rightarrow\quad \left(\tau_{\xi\eta}\right)_{296,n} = -\left(\tau_{\xi\eta}\right)_{294,n} \tag{28}$$

$$\left(\frac{\partial\tau_{\xi\eta}}{\partial\varepsilon}\right)_{296,n} = \left(\frac{\partial\tau_{\xi\eta}}{\partial\varepsilon}\right)_{294,n} \tag{29}$$

$$\left(\frac{\partial\sigma_y}{\partial\varepsilon}\right)_{296,n} = \left(\frac{\partial\sigma_y}{\partial\varepsilon}\right)_{294,n} \tag{30}$$

The geometric interpretation of the horizontal and vertical positions and rotations of the first several connecting elements, along with the excitation at the base, are shown in Figure 11. The horizontal and vertical coordinates of point k at time step n, $X_{k,n}$ and $Y_{k,n}$, depend on the displacement of the elements below it. Let $\varepsilon_{k,n}$ be the rotation of the connecting element between two points k and $k+1$ (Figure 9). Then, the connection between the elements (Figure 11) implies

$$X_{k,n} = \left(U_g\right)_{1,n} + \sum_{j=1}^{k-1}\left(dy\sin\varepsilon_{j,n}\right) \tag{31}$$

$$Y_{k,n} = \left(V_g\right)_{1,n} + \sum_{j=1}^{k-1}\left[dy\left(\cos\varepsilon_{j,n} - 1\right)\right] \tag{32}$$
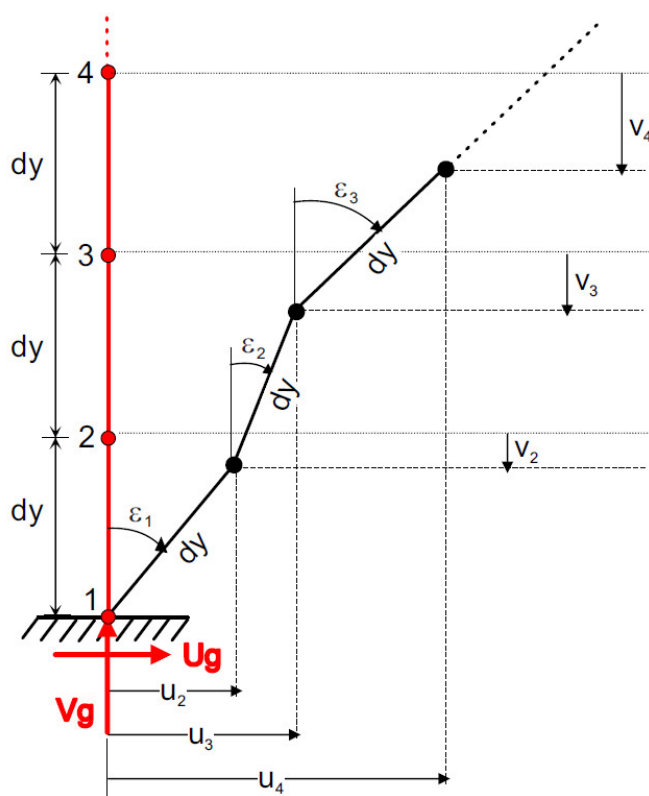
Figure 11. Horizontal and vertical displacements and rotations of the model.

3. Results

3.1. Qualitative Calibration

We employ the observed damage in VN7SH only as a qualitative guide about the cases that may be of interest to explore. We did not attempt to model its response in realistic detail, which would require specific modeling of the structure and result in many response complexities that would make causal interpretation of the final results difficult. As the nonlinear problems had highly variable outcomes and depended on real-time interaction between the initial conditions, excitation, and nonlinear response, the outcome could thus be described only by distributions, with no possibility of unique deterministic results.

We began by using the recorded motions at the base of the building (Figure 5) to select strong-motion "excitation" consisting of five strong-motion pulses. The pulse amplitudes ranged from 7 to 12 cm, and the durations lasted from 1.4 to 2.4 s. As in Figure 5, we assumed those five pulses all acted in the same direction and at the times corresponding to the times seen in the figure. We calculated the permanent strains in our model and showed their distribution along the model height after each pulse in Figure 12.
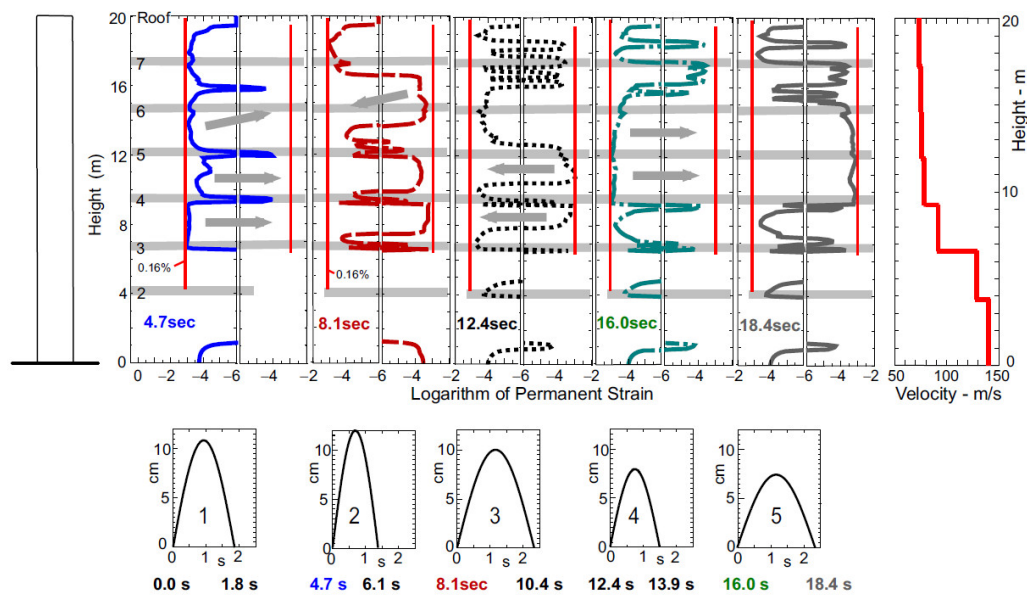
Figure 12. The permanent strains in the building model resulting from a sequence of five pulses (pulses start at 0.0 s, 4.7 s, 8.1 s, 12.4 s, and 16.0 s). Strains are shown during the quiescent ground-motion times—before the onset of the following pulses (before 4.7 s, 8.1 s, 12.4 s, and 16.0 s) and after the fifth pulse at 18.4 s. Vertical red lines labeled 0.16% show that the permanent strains did not exceed this value.

In this example, all five pulses act in the same direction. Thus, although it might be expected that the permanent strains would progressively increase after each pulse, this was not the case. As Figure 12 shows, between the third and seventh floors (between 7-m and 16-m heights), permanent strains changed the sign. For example, after the second pulse, three areas with large, negative permanent strains became permanent positive strains of comparable amplitudes. During the last, fifth pulse, a similar reversal occurred. Perusal of the sequence of such changes shown in Figure 12 confirms that the principle of superposition did not apply in nonlinear problems.

Figure 12 also shows that the reversals of positive and negative permanent strains were approximately centered near the fifth floor where the main damage occurred during the Northridge earthquake (Figure 4). Furthermore, Figure 12 shows that during this particular excitation, the amplitudes of the permanent strain did not increase during excitation by five pulses. The peak permanent strains reached amplitudes of about 0.16% after excitation by the first pulse, and as shown in the figure by the labeled vertical lines at 0.16%, did not exceed this amplitude during the second and all subsequent pulses.

3.2. An Example of Collapse

As can be seen from Figure 5, the EW pulses in strong-ground motion during the Northridge earthquake did not exceed about 12 cm, and while these amplitudes did damage the building, it did not collapse. To illustrate a collapsing behavior of the shear-beam model building, the displacement pulses were amplified 14 times. Thus, in the following A_1 = 154 cm, A_2 = 168 cm, A_3 = 140 cm, A_4 = 112 cm, and A_5 = 98 cm were used as amplitudes of successive pulses, and the pulse durations of 1.8, 1.4, 2.3, 1.5, and 2.4 s were kept the same. These amplitudes and durations were not intended to model any specific measured earthquake displacement, and their purpose was only to illustrate one hypothetical example, which would lead to a complete collapse of the model building in this paper. Nevertheless, these amplitudes were of the same order as what could be expected in the vicinity of faults breaking the surface in California.

In this example, the collapse occurred at the end of excitation, just after the end of the fifth pulse. For larger amplitudes, the collapse occurred earlier; however, a detailed analysis and description of such cases was beyond the scope of this paper. In the example considered here, the building experienced progressively increasing permanent strains, which would bring it to a rapid collapse after the action of the last pulse, at 18.4 s.

In contrast with Figure 12, which shows reversals of signs of the permanent strains, and in spite of the fact that all five pulses acted in the same direction, Figure 13 shows increasing permanent strains, all in the same direction, and a large sign reversal at 18.4 s, just before collapse.
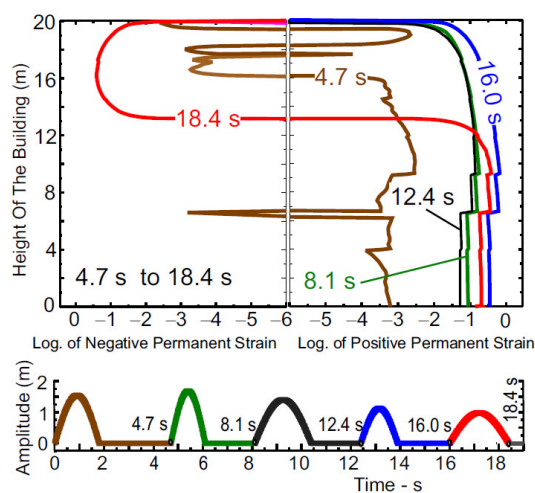

Figure 13. Permanent strains in the building model resulting from a sequence of five pulses. Strains are shown for times during quiescent ground motion just before the onset of the following pulses (at 4.7 s, 8.1 s, 12.4 s, and 16.0 s) and after the fifth pulse at 18.4 s.

Figure 14 shows the displacements along the building height during excitation by the first three pulses. During the first pulse, the drift amplitudes were already much larger than 1%, and during the response to the second and third pulses, the drifts exceeded 10%. These were large displacements that exceed the threshold of tolerable drift amplitudes [46]. Although the building was severely damaged, it was still standing.
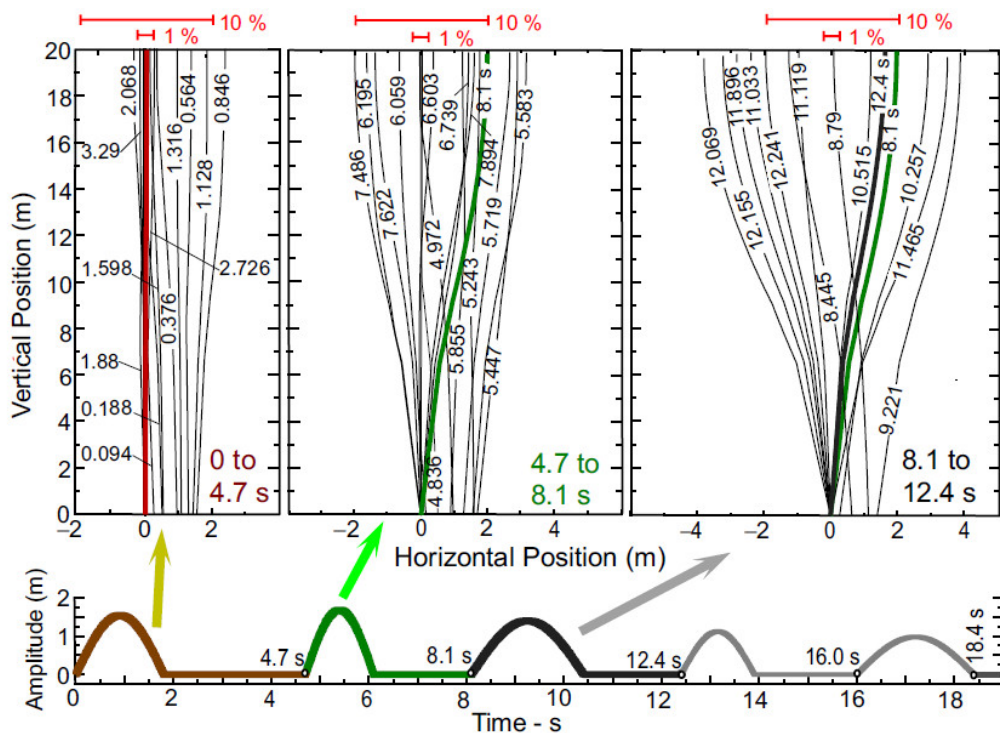
Figure 14. Model displacements during the first three pulses, which, after the third pulse, exceed a 10% drift. Roof displacements corresponding to 1% and 10% drifts are shown with red lines above the figure. Consecutive displacements of the building are shown during the first three pulses. The duration times corresponding to the plotted configuration are shown in seconds.

During the action of the last two pulses, between 12.4 s and 18.4 s, the building displacements still oscillated, but with progressively larger displacements, corresponding to and exceeding drifts of 20% (Figure 15). Then, between 18.4 s and 18.742 s, gravity forced the building to rapidly fall. The collapse occurred between 18.742 s and 18.763 s. Figure 16 shows the evolution of permanent strains during the beginning of collapse, while the building swings through the vertical from right to left as shown in Figure 17 (left). Figure 17 (right) shows the very last stages of collapse beginning at 18.742 s and then the final collapse at 18.763 s.
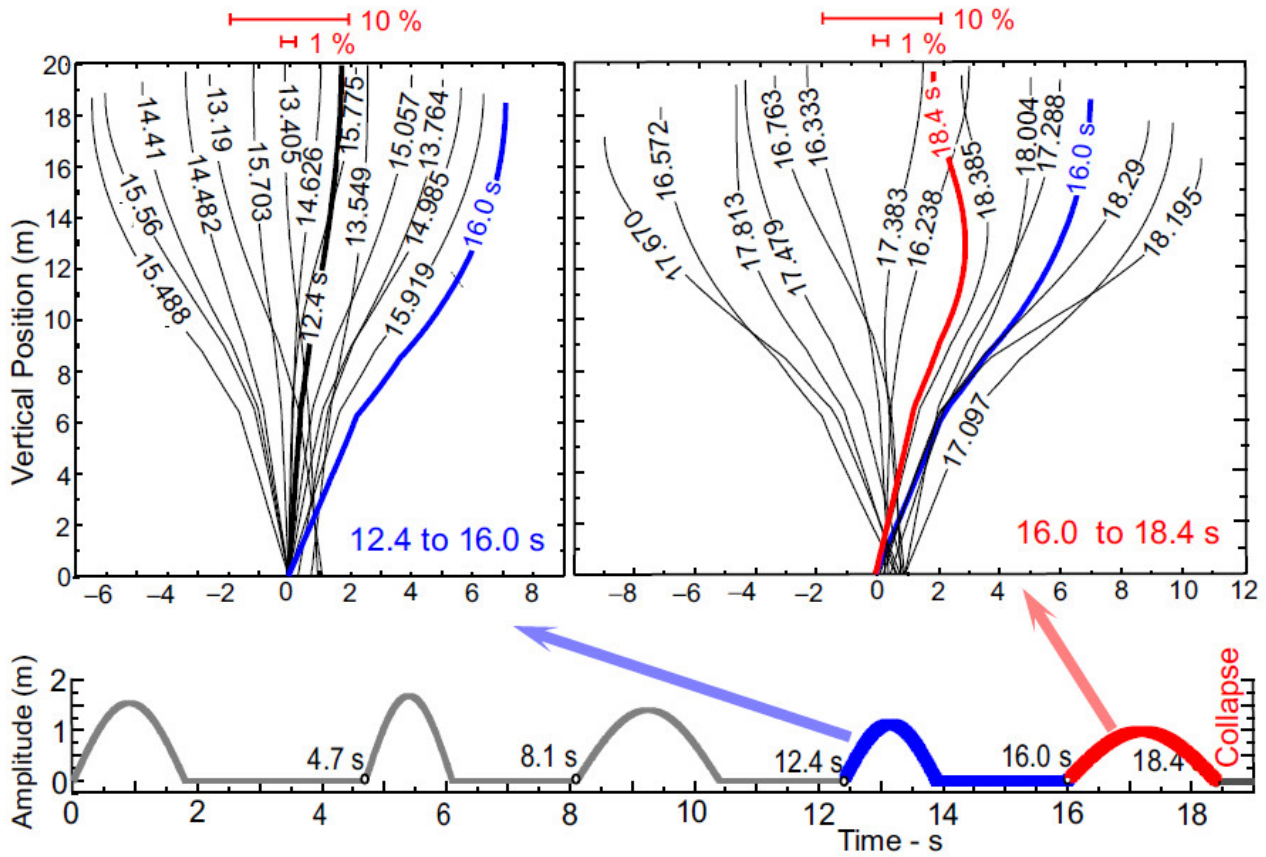
Figure 15. Model displacements during the last two pulses. The roof displacements corresponding to 1% and 10% drifts are shown in red lines above the figure. Consecutive displacements of the building are shown during the last two pulses. The duration times corresponding to the plotted configuration are shown in seconds.

In this example, we assumed only the horizontal ground motion, and thus the final approach to collapse, between 18.4 s and 18.763 s, was dominated by the action of gravity. Consideration of the vertical and rocking ground motions would have resulted in a more complex sequence dominated by dynamic instability, especially when the vertical pulse ground motion acted in the upward direction.
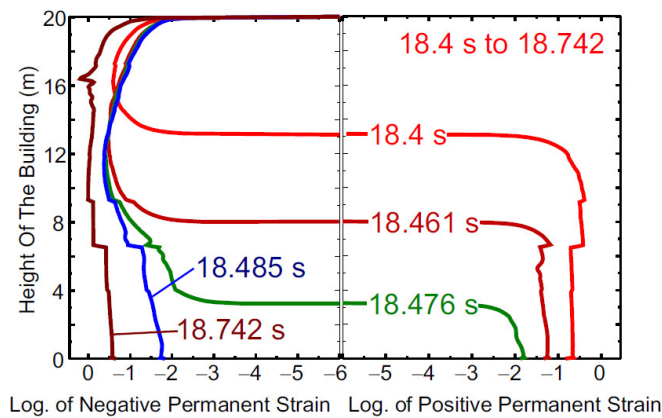
Figure 16. Permanent strains in the building model after the fifth pulse, during the short time interval from 18.4 s to 18.742 s. The evolution of permanent strains during the time just preceding the collapse of the building, is shown, which occurs after 18.742 s.
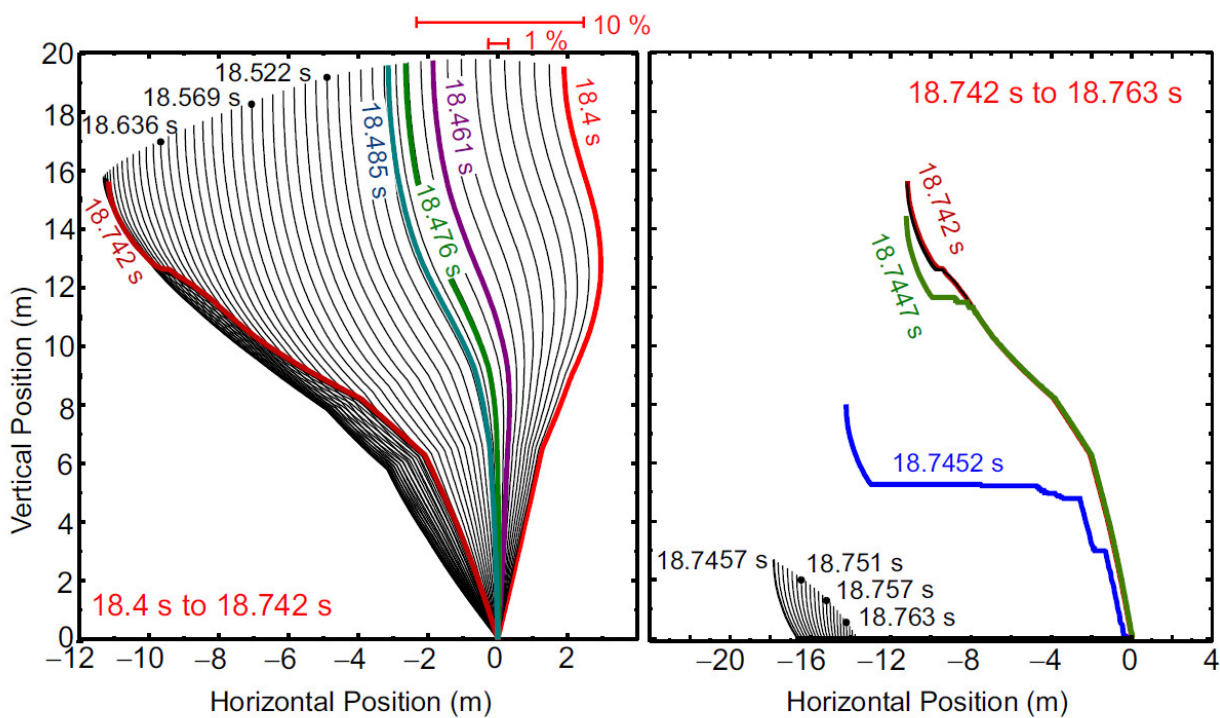
Figure 17. Movement of the building just before the final collapse (**left**), and the rapid collapse sequence between 18.742 s and 18.763 s (**right**).

4. Discussion and Conclusions

In this paper, we introduced a nonlinear model of a shear beam building that could collapse as a result of the action of large horizontal displacements at its base and with full participation of the gravity force. To make the examples of nonlinear response plausible, the ground-motion pulses used in the examples were selected to resemble the ground motion recorded at a building site in the central San Fernando Valley during the 1994 earthquake in Northridge, California.

Most contemporary approaches for analyses of collapsing structural response require sudden removal of one or several key structural-bearing members in order to initiate failure [1–8]. In contrast, the model we describe in this paper requires no such causal initiation. The model naturally begins to experience large strains and dynamic instabilities wherever and whenever the wave motion in the structure initiates large nonlinear deformations and unstable configuration. Further refinement and generalization of such a modeling approach will be invaluable for structural-response analyses and collapse mechanisms during other catastrophic events that are associated with extremely large loads (high winds, heavy debris carried by tsunami inundation, projectile loading and penetration, above-and-within ground explosions, collisions with heavy objects, and many others).

Our aim was not to analyze in detail whether and under what conditions VN7SH would have collapsed were it excited by larger ground motion—for example, somewhere near or at an earthquake fault. Such an analysis requires more detailed modeling of the building, the consideration of all ground-motion components and the modeling of the soil–structure interaction effects. Nevertheless, our analysis suggests that the approach described in this paper can be generalized to predictions of nonlinear and collapsing ranges of response, both in the range of motions that were recorded at the VN7SH site during the Northridge earthquake and during far greater ground-motion amplitudes that can be expected to occur near surface breaks of earthquake faults.

Systematic further development of the analysis methods of the collapsing stage of response of buildings will make it possible to devise new design strategies, which will be introduced to delay and prevent collapse. This will require numerous sensitivity studies and the systematic interpretation of a great many possible outcomes. Monitoring the dissipated energy of nonlinear responses will provide a tool for more realistic design methods. Such methods will move away from response spectra and toward balancing the time history of demand power of strong motion with the capacity of structures to absorb the energy during large nonlinear responses.

The shear beam model we considered in this paper is suitable for buildings with large plan dimensions and with only moderate heights. For modern tall buildings, the overall contribution of bending deformations will have to be considered, either as a Timoshenko beam [21], or as coupled Bernoulli and shear beams [47,48]. Such improvements and generalizations will be addressed in our future work.

References

1. Adam, J.M.; Parisi, F.; Sagaseta, J.; Li, X. Research and practice on progressive collapse and robustness of building structures in the 21st century. *Eng. Struct.* **2018**, *173*, 122–149.
2. Sharafi, P.; Alembagheri, M.; Kildashti, K.; Ganji, H.T. Gravity-induced progressive collapse response of precast corner-supported modular buildings. *J. Archit. Eng.* **2021**, *27*, 04021031.
3. Thai, H.-T.; Ho, Q.V.; Li, W.; Ngo, T. Progressive collapse and robustness of modular high-rise buildings. *Struct. Infrastruct. Eng.* **2021**, *19*, 302–314.
4. Alembagheri, M.; Sharafi, P.; Hajireazei, R.; Tao, Z. Anti-collapse resistance mechanisms in corner-supported modular steel buildings. *J. Constr. Steel Res.* **2020**, *170*, 106083.
5. Hadi, M.N.S. New building scheme to resist progressive collapse. *J. Archit. Eng*. **2012**, *18*, 1–8.
6. Manie, S.; Moghadam, A.S.; Ghafory-Ashtiany, M. Collapse behavior evaluation of asymmetric buildings subjected to bi-directional ground motion. *Struct. Des. Tall Spec. Build.* **2015**, *24*, 607–628.
7. Song, B.; Sezen, H. Experimental and analytical progressive collapse assessment of steel frame building. *Eng. Struct.* **2013**, *56*, 664–672.
8. Fang, C.; Linzell, D. Examining progressive collapse robustness of a high-rise reinforced concrete building. *Eng. Struct.* **2021**, *248*, 113274.
9. Trifunac, M.D. 75th Anniversary of strong motion observation—A historical review. *Soil Dyn. Earthq. Eng.* **2009**, *29*, 591–606.
10. Todorovska, M.I.; Trifunac, M.D. Impulse response analysis of the Van Nuys 7-story hotel during 11 earthquakes and earthquake damage detection. *Struct. Control Health Monit.* **2008**, *15*, 90–116.
11. Todorovska, M.I.; Trifunac, M.D. Earthquake damage detection in Imperial County Services Building II: Analysis of novelties via wavelets. *Struct. Control. Health Monit.* **2010**, *17*, 895–917.
12. Trifunac, M.D.; Ivanović, S.S.; Todorovska, M.I. Apparent periods of a building I: Fourier analysis. *J. Struct. Eng.* **2001**, *127*, 517–526.
13. Trifunac, M.D.; Ivanović, S.S.; Todorovska, M.I. Apparent periods of a building II: Time-frequency analysis. *J. Struct. Eng.* **2001**, *127*, 527–537.
14. Housner, G.W.; Trifunac, M.D. Analysis of accelerograms-Parkfield Earthquake. *Bull. Seismol. Soc. Am.* **1967**, *57*, 1193–1220.
15. Trifunac, M.D. Tectonic stress and source mechanism of the Imperial Valley, California earthquake of 1940. *Bull. Seismol. Soc. Am*. **1972**, *62*, 1283–1302.
16. Trifunac, M.D. A three-dimensional dislocation model for the San Fernando, California, earthquake of February 9, 1971. *Bull. Seismol. Soc. Am*. **1974**, *64*, 149–172.

17. Wald, D.J.; Heaton, T.H. The slip history of the 1994 Northridge, California, earthquake determined from strong-motion, teleseismic, GPS and leveling data. *Bull. Seismol. Soc. Am.* **1996**, *86*, S49–S70.

18. Trifunac, M.D.; Ivanović, S.S.; Todorovska, M.I. *Instrumented 7-Storey Reinforced Concrete Building in Van Nuys, California: Description of Damage from the 1994 Northridge Earthquake and Strong Motion Data*; Report CE 99-02; Department of Civil Engineering, University of Southern California: Los Angeles, CA, USA, 1999.

19. Todorovska, M.I. Soil-structure system identification of Millikan Library North-South response during four earthquakes (1970–2002): What caused the observed wandering of the system frequencies? *Bull. Seismol. Soc. Am.* **2009**, *99*, 626–635.

20. Rahmani, M.; Ebrahimian, M.; Todorovska, M.I. Time-wave velocity analysis for early earthquake damage detection in buildings: Application to a damaged full-scale RC building. *Earthq. Eng. Struct. Dyn.* **2015**, *44*, 619–636.

21. Rahmani, M.; Todorovska, M.I. Structural health monitoring of a 32-story steel moment-resisting frame building using 50 years of seismic monitoring data. *Earthq. Eng. Struct. Dyn.* **2021**, *50*, 777–1800.

22. Gičev, V.; Trifunac, M.D. Permanent deformations and strains in a shear building excited by a strong motion pulse. *Soil Dyn. Earthq. Eng.* **2007**, *27*, 774–792.

23. Gičev, V.; Trifunac, M.D. Transient and permanent shear strains in a building excited by strong earthquake pulses. *Soil Dyn. Earthq. Eng.* **2009**, *29*, 1358–1366.

24. Gičev, V.; Trifunac, M.D. A note on predetermined earthquake damage scenarios for structural health monitoring. *Struct. Control Health Monit.* **2012**, *19*, 746–757.

25. Ivanović, S.S.; Trifunac, M.D.; Novikova, E.I.; Gladkov, A.A.; Todorovska, M.I. *Instrumented 7-Storey Reinforced Concrete Building in Van Nuys, California: Ambient Vibration Surveys Following the Damage from the 1994 Northridge Earthquake*; Report CE 99-03; Department of Civil Engineering, University of Southern California: Los Angeles, CA, USA, 1999.

26. Trifunac, M.D.; Ivanović, S.S.; Todorovska, M.I.; Novikova, E.I.; Gladkov, A.A. Experimental evidence for flexibility of a building foundation supported by concrete friction piles. *Soil Dyn. Earthq. Eng.* **1999**, *18*, 169–187.

27. Ivanović, S.S.; Trifunac, M.D.; Novikova, E.I.; Gladkov, A.A.; Todorovska, M.I. Ambient vibration tests of a seven-story reinforced concrete building in Van Nuys, California, damaged by the 1994 Northridge Earthquake. *Soil Dyn. Earthq. Eng.* **2000**, *19*, 391–411.

28. Ivanović, S.S.; Trifunac, M.D.; Todorovska, M.I. On identification of damage in structures via wave travel times. In Proceedings of the Nato Advanced Research Workshop on Strong-Motion Instrumentation for Civil Engineering Structures, Istanbul, Turkey, 2–5 June 1999; Kluwer Academic Publ.: Dordrecht, The Netherland, 2001; pp. 447–468.

29. Trifunac, M.; Hao, T.Y. *7-Storey Reinforced Concrete Building in Van Nuys, California: Photographs of the Damage from the 1994 Northridge Earthquake*; Report CE 01-05; Department of Civil Engineering, University of Southern California: Los Angeles, CA, USA, 2001.

30. John A. Blume Associates. *Holiday Inn, in San Fernando, California, Earthquake of February 9, 1971*; Murphy, L.M., Ed.; U.S. Department of Commerce, National Oceanic and Atmospheric Administration: Washington, DC, USA, 1973.

31. Mulhern, M.R.; Maley, R.P. *Building Period Measurements before, during and after the San Fernando, California, Earthquake of February 9, 1971*; U.S. Department of Commerce, National Oceanic and Atmospheric Administration: Washington, DC, USA, 1973; Volume I, Part B, pp. 725–733.

32. Browning, J.A.; Li, R.Y.; Lynn, A.; Moehle, J.P. Performance assessment for a reinforced concrete frame building. *Earthq. Spectra* **2000**, *16*, 541–555.

33. De la Llera, J.C.; Chopra, A.K.; Almazan, J.L. Three-dimensional inelastic response of an RC building during the Northridge earthquake. *J. Struct. Eng.* **2001**, *127*, 482–489.

34. Islam, M.S. *Analysis of the Response of an Instrumented 7-Story Non Ductile Concrete Frame Building Damaged during the Northridge Earthquake*; Professional Paper 96-9; Los Angeles Tall Buildings Structural Design Council: Los Angeles, CA, USA, 1996.

35. Li, Y.R.; Jirsa, J.O. Nonlinear analyses of an instrumented structure damaged in the 1994 Northridge earthquake. *Earthq. Spectra* **1998**, *14*, 265–283.

36. Trifunac, M.D.; Ivanović, S.S. *Analysis of Drifts in a Seven-Story Reinforced Concrete Structure*; Report No. CE 03-01; Department of Civil Engineering, University of Southern California: Los Angeles, CA, USA, 2003.

37. Trifunac, M.D.; Todorovska, M.I. Nonlinear soil response as a natural passive isolation mechanism—The 1994 Northridge, California earthquake. *Soil Dyn. Earthq. Eng.* **1998**, *17*, 41–51.

38. Trifunac, M.D.; Todorovska, M.I. Damage distribution during the 1994 Northridge, California, earthquake in relation to generalized categories of surficial geology. *Soil Dyn. Earthq. Eng.* **1998**, *17*, 239–253.

39. Trifunac, M.D.; Todorovska, M.I.; Ivanović, S.S. Peak velocities, and peak surface strains during Northridge, California, earthquake of 17 January 1994. *Soil Dyn. Earthq. Eng.* **1996**, *15*, 301–310.

40. Trifunac, M.D.; Todorovska, M.I. Northridge, California, earthquake of 17 January 1994: Density of pipe breaks and surface strains. *Soil Dyn. Earthq. Eng.* **1997**, *16*, 193–207.

41. Trifunac, M.D.; Todorovska, M.I. Northridge, California, earthquake of 1994: Density of red-tagged buildings versus peak velocity and intensity of shaking. *Soil Dyn. Earthq. Eng.* **1997**, *16*, 209–222.

42. Trifunac, M.D.; Todorovska, M.I. Reduction of structural damage by nonlinear soil response. *J. Struct. Eng.* **1999**, *125*, 89–97.

43. Trifunac, M.D.; Todorovska, M.I.; Ivanović, S.S. A note on distribution of uncorrected peak ground accelerations during the Northridge, California, earthquake of 17 January 1994. *Soil Dyn. Earthq. Eng.* **1994**, *13*, 187–196.

44. Shakal, A.; Huang, M.; Darragh, R.; Cao, T.; Sherburne, R.; Malhotra, P.; Cramer, C.; Syndov, R.; Graizer, V.; Maldonado, G.; et al. *CSMIP Strong-Motion Records from the Northridge, California, Earthquake of 17 January 1994*; Report No. OSMS 94-07; California Department of Conservation, Division of Mines and Geology: Sacramento, CA, USA, 1994.

45. Lax, P.D.; Wendroff, B. Difference schemes for hyperbolic equations with high order of accuracy. *Comm. Pure Appl. Math.* **1964**, *17*, 381–398.

46. Ghobarah, A. On drift limits associated with different damage levels. In Proceedings of the International Workshop on Performance-Based Seismic Design, Bled, Slovenia, 28 June–1 July 2004; pp. 321–332.

47. Alonso Rodriguez, A.; Miranda, E. Assessment of building behavior under near-fault pulse-like ground motions through simplified methods. *Soil Dyn. Earthq. Eng.* **2015**, *29*, 47–58.

48. Meza Fajardo, K.; Papageorgiou, A.S. Ductility demands of tall buildings subjected to base rocking induced by Rayleigh waves. *Earthq. Eng. Struct. Dyn.* **2019**, *48*, 1174–1194.